

Influence of Iron Microstructure on Corrosion Inhibitor Performance in Acidic Media

E. E. Oguzie,^{*,†,‡} S. G. Wang,[§] Y. Li,^{*,†} and F. H. Wang[†]

State Key Laboratory for Corrosion and Protection, Institute of Metal Research, Chinese Academy of Sciences, 62 Wencui Road, Shenyang 110016, China, Shenyang National Laboratory for Materials Sciences, Institute of Metal Research and International Centre for Materials Physics, Chinese Academy of Sciences, 72 Wenhua Road, Shenyang 110016, China, and Electrochemistry and Materials Science Research Laboratory, Department of Chemistry, Federal University of Technology Owerri, PMB 1526, Owerri, Nigeria

Received: February 19, 2009; Revised Manuscript Received: April 2, 2009

Electrochemical measurements employing ac and dc techniques as well as atomic force microscopy were used to study the electrochemical corrosion behavior of ingot iron with two different microstructures: conventional polycrystalline ingot iron (CPII) and bulk nanocrystalline ingot iron (BNII) fabricated from CPII by severe rolling, without and with inhibitors. The corrosive media was 0.1 M H₂SO₄ solution, while thiourea (TU) was employed as inhibitor, with a concentration of 5.0 mM, as well as a 1:1 combination of TU and KI. Impedance and polarization results show that BNII was more susceptible to corrosion in the uninhibited acid. The presence of TU improved the corrosion resistance of both specimens comparably, while KI reduced the inhibition efficiency of TU. Infrared spectrophotometry revealed that the interfacial species for CPII and BNII in the presence of TU were quite identical and markedly different from that in TU + KI. Molecular dynamics (MD) simulations were performed to illustrate the adsorption process of TU at a molecular level, and the theoretical predictions showed good agreement with the electrochemical results.

1. Introduction

There is no doubt that the use of corrosion inhibitors remains an inexpensive and effective method for corrosion control in aqueous aggressive environments. The corrosion inhibiting effect of organic molecules is often attributed to their adsorption on the corroding metal surface, thereby creating a barrier which isolates the metal from the corrodent. The effectiveness of inhibition then depends on the chemical, electrical, and structural characteristics of the adsorbed inhibitor layer, which in turn depend strongly on such factors as the inhibitor structure and concentration and the nature of the metal surface including the population of potential adsorption sites as well as the temperature and composition of the aggressive environment. Due to the complex nature of the corrosion process including the specificity of action of most inhibitors, combinations of inhibiting additives have proved to be more effective and practical means for corrosion control. Combination of some organic inhibitors with halide ions has been reported to yield useful enhancements in inhibition efficiency.^{1–8} The tendency of halide ions to become specifically adsorbed on a corroding metal surface has been long recognized. The adsorbed ions then attract the inhibitor electrostatically into the Helmholtz electrical double layer, leading to cooperative (synergistic) adsorption which increases the degree of surface coverage. Most such studies, however, often assume that the characteristics of the additives remain chemically unaltered on adsorption, i.e., no significant chemical or electronic interactions between the additives, apart from the electrostatic interactions responsible for the observed cooperative effect. Such assumption may, however, be mislead-

ing in certain circumstances, considering that only very few studies actually investigated the nature of the halide–organic inhibitor film.

These days, grain size modification by nanocrystallization is generating a lot of interest as a means of improving materials corrosion performance. Nanocrystalline metals and alloys have been extensively investigated because of the need for better understanding of the nanostructure, vis-à-vis the structural and chemical stability as well as potential technological applications. Nevertheless, there is still no generally acceptable consensus as to the precise relationship between grain size and corrosion resistance at a fundamental level, as the effect of nanocrystallization on corrosion performance is neither uniform nor definite but varies according to the nature of the material and environment and could lead to either improved^{9–11} or reduced^{12,13} corrosion resistance. Again, the effect of the nanocrystalline microstructure on corrosion inhibitor performance has not received much attention.

In the present study, we assess the effect of grain size on the rate at which metals may corrode in the active region as well as on the protective effect of any added corrosion inhibiting additive. As an extension of our earlier studies,^{14–17} we continue focus on pure (ingot) iron, this time in 0.1 M H₂SO₄ solution, with thiourea (TU) as corrosion inhibitor. Thiourea and its derivatives have been widely studied as an effective class of corrosion inhibiting additives for different metals and alloys.^{18–22} However, a key feature of TU is its sensitivity to variations in the test environment as well as the nonregular relationship between concentration and inhibition efficiency. The progressive disappearance of the inhibiting effect at [TU] ≥ 10 mmol/L has been attributed to factors such as protonation of TU and reduction of TU to corrosion promoting particles such as HS[–] ion.²² Again, little attention has been given to the influence of halide ions on the inhibiting effect of TU. Accordingly, we have

* Corresponding authors. E-mail address: emekaoguzie@gmail.com (E.E.O.); liying@imr.ac.cn (Y.L.).

[†] Institute of Metal Research, Chinese Academy of Sciences.

[‡] Federal University of Technology Owerri.

[§] Institute of Metal Research and International Centre for Materials Physics, Chinese Academy of Sciences.

examined the inhibiting effect of TU + KI combinations, in comparison with TU alone.

2. Experimental Section

Our experimental approach involved assessment of the electrochemical behavior of the metal specimens and the inhibitor film by electrochemical impedance spectroscopy and potentiodynamic polarization. Atomic force microscopy (AFM) was used to provide a direct visualization of the corrosion morphology of the metal surfaces in inhibited and uninhibited solution, while infrared spectroscopy (FTIR) was used to characterize the interfacial species formed on the metal surfaces in different inhibitor systems.

The test specimens used in this study were a conventional polycrystalline ingot iron (CPH) and bulk nanocrystalline ingot iron (BNH). BNH was prepared from CPH by the severe rolling technique. The details of the severe rolling technique and subsequent microstructure characterization of CPH and BNH have been described elsewhere.¹⁴ The specimens were machined into test coupons of dimension 1 cm × 1 cm, which were wet-polished with silicon carbide abrasive paper (from grade #600 to #1000), degreased in acetone, rinsed with distilled water, and dried in warm air. The test electrolyte was 0.1 M H₂SO₄, prepared from analytical reagent grade concentrated acid using distilled water. Corrosion tests were carried out in the blank corrodent, without and with 0.005 M solutions of the test inhibitor, thiourea (TU). The effect of iodide ions was assessed by introducing 0.005 M KI into inhibited solutions containing TU.

Electrochemical experiments were performed using a PARC Parstat-2273 Advanced Electrochemical System operated with Powercorr and Powersine software. A conventional three-electrode glass cell was used for the experiments. Test coupons with 1 cm² exposed surface area were used as working electrode and a platinum foil as counter electrode. The reference electrode was a saturated calomel electrode (SCE), which was connected via a Luggin's capillary. The working electrode was immersed in a test solution for 1 h to attain a stable open circuit potential, after which potentiodynamic polarization studies were carried out in the potential range −1100 to 400 mV at a scan rate of 0.333 mV s^{−1}. Electrochemical impedance spectroscopy (EIS) measurements were made at corrosion potentials (E_{corr}) over a frequency range of 100 kHz–10 mHz, with a signal amplitude perturbation of 5 mV. Spectra analyses were performed using Zsimpwin software, also supplied by PARC. All experiments were undertaken in 300 mL of stagnant aerated solutions at 30 ± 1 °C.

Morphological studies of the mild steel electrode surface were undertaken by atomic force microscopy, AFM (PicoPlus Scanning Probe Microscope, Molecular Imaging Corp.). AFM images were realized in tapping mode at room temperature. Test metal specimens were immersed for 3 h in 0.1 M H₂SO₄ without and with 0.005 M TU, respectively, at 30 ± 1 °C, then washed with distilled water, dried in warm air, and submitted for AFM surface examination. AFM images of the uncorroded specimens were also obtained after further polishing with diamond paste.

Fourier transform infrared (FTIR) spectra (KBr pellet) were recorded using a Nicolet-Magna-IR 560 FTIR spectrophotometer. The spectra for the protective film in TU as well as TU + KI were recorded by carefully removing the film, mixing it with KBr, and making the pellet.

All theoretical calculations were performed using the density functional theory (DFT) electronic structure programs Forcite and DMol³ as contained in the Materials Studio 4.0 software.

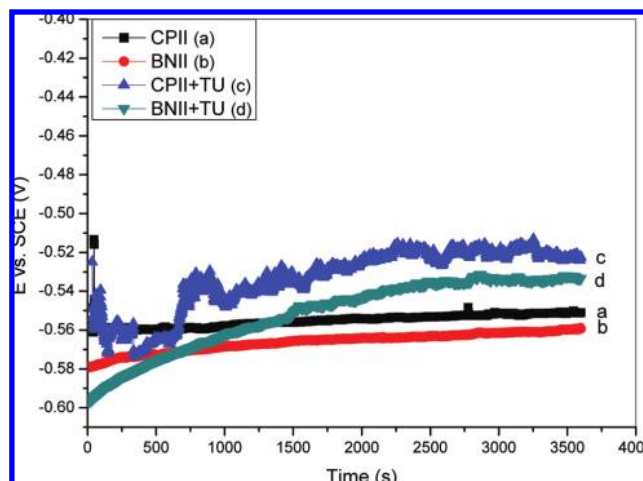


Figure 1. Variation of open-circuit potential (OCP) with time for CPH and BNH in 0.1 M H₂SO₄ without and with TU.

3. Results and Discussion

3.1. Electrochemical Corrosion Behavior of CPH and BNH. Open-Circuit Potential Measurements. The evolutions of the open-circuit potential (OCP) with time for the two-iron specimen in 0.1 M H₂SO₄ without and with addition of 0.005 M TU are shown in Figure 1. The OCP of both specimens stabilized within 1 h. Though the difference in OCP is not very great, the attained OCP values for BNH were always lower (more negative), indicating that BNH presents a more active corrosion surface. This could be related to the microstructural differences between both specimens vis-à-vis the grain sizes and grain boundary population. The difference in surface morphology is obvious from the AFM images of the uncorroded specimens presented in Figure 2. Mean grain sizes of 50 μm (CPH) and 39 nm (BNH) had been previously established.¹⁴ BNH with smaller grain size and higher population of grain boundaries provides a greater surface area for interaction with the corrodent, hence a higher population of active sites for the corrosion reaction.

Impedance Measurements. Impedance experiments were undertaken to afford insight into the characteristics and kinetics of electrochemical processes occurring at the CPH/0.1 M H₂SO₄ and BNH/0.1 M H₂SO₄ interfaces. Figure 3a shows the impedance response of both specimens measured at OCP after 30 min of immersion in uninhibited acid. The Nyquist plots for both specimens generally have the form of only one depressed semicircle in the high frequency region, which denotes that the process is under charge-transfer control and corresponds to one time constant. The single time constant may be attributed to the short exposure time in the corrodent, which is insufficient to reveal degradation of the substrate.²³ The depression of the Nyquist semicircle with center under the real axis is typical for solid metal electrodes that show frequency dispersion of the impedance data. The transfer function can be represented by a solution resistance R_s , shorted by a capacitor (C) that is placed in parallel to the charge-transfer resistance R_{ct} .²⁴

$$Z_{(\omega)} = R_s + \left(\frac{1}{R_{\text{ct}}} + j\omega C \right)^{-1} \quad (1)$$

This transfer function is, however, only applicable for homogeneous systems with one time constant when the center of the semicircle lies on the abscissa and cannot account for the depression of the capacitive semicircle. When a nonideal frequency response is present, the capacitor is replaced by a

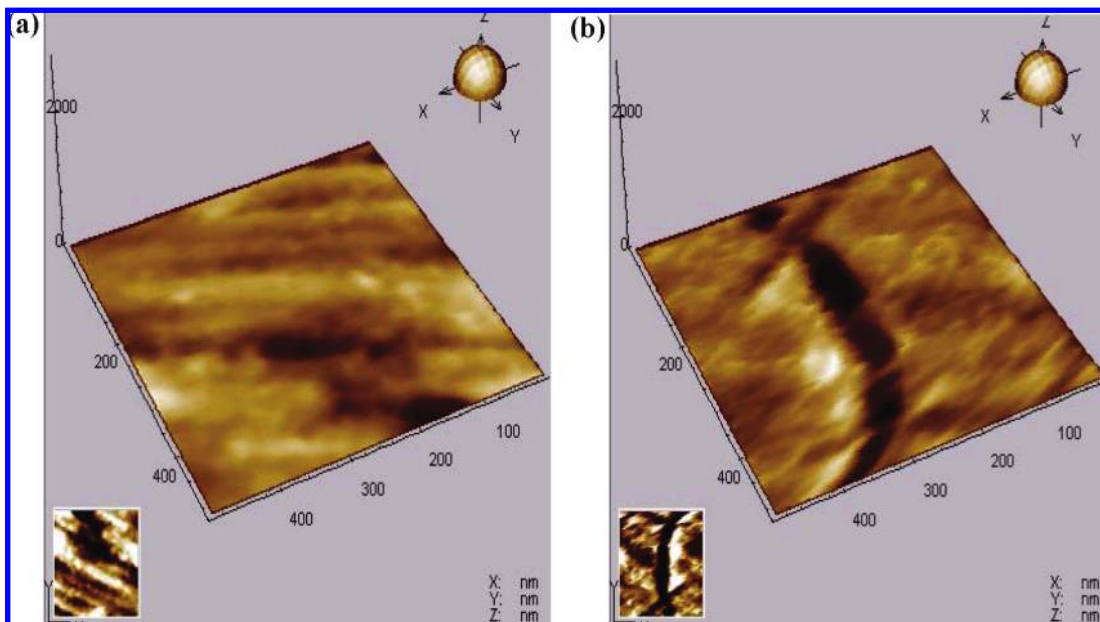


Figure 2. AFM images of the as-polished (a) CPII and (b) BNII surfaces.

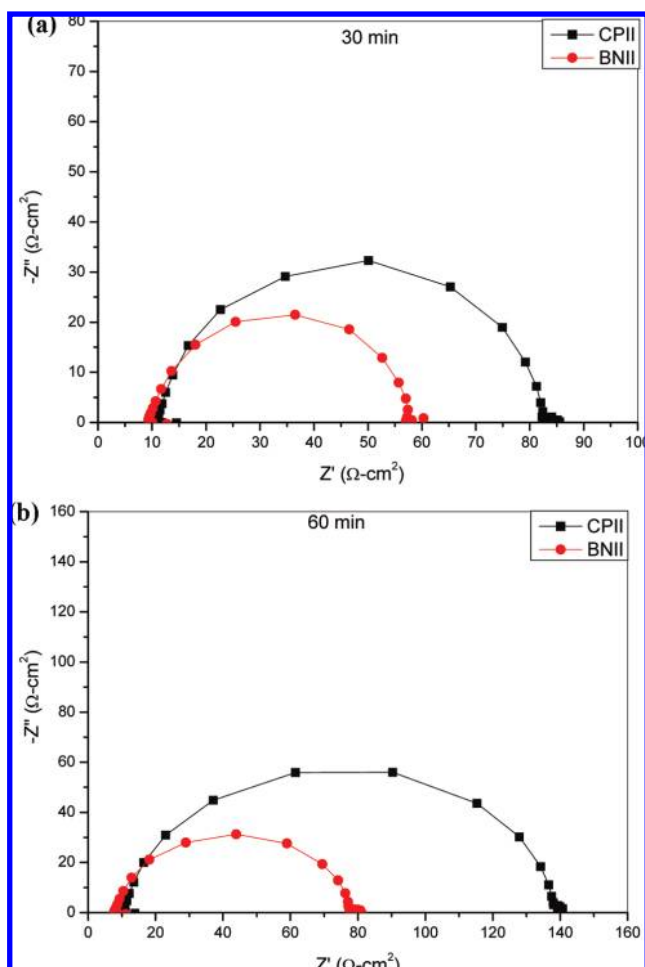


Figure 3. EIS Nyquist plots of CPII and BNII in 0.1 M H₂SO₄ after immersion for (a) 30 min and (b) 60 min.

constant phase element (CPE). The use of such a CPE accounts for the deviations from ideal dielectric behavior and

is related to surface inhomogeneities. The impedance, Z , of the CPE is²⁵

$$Z_{\text{CPE}} = Q^{-1}(j\omega)^{-n} \quad (2)$$

where Q and n stand for the CPE constant and exponent, respectively, $j = (-1)^{1/2}$ is an imaginary number, and ω is the angular frequency in rad s⁻¹ ($\omega = 2\pi f$), when f is the frequency in Hz.

The impedance plots for CPII and BNII after 60 min of immersion are presented in Figure 3b. Compared to the results in Figure 3a, the impedance and hence corrosion resistance of both samples increased with time, with R_{ct} values increasing from 73.2 to 127.6 Ω-cm² for CPII and 48.0 to 70.3 Ω-cm² for BNII. This can be attributed to the slow adsorption of reaction products at dissolution sites and consequent decrease in corrosion rate.²⁶ The close similarity between the two impedance spectra over the frequency range studied is a clear indication that the nanostructured specimen behaves electrochemically as the conventional Fe. Nevertheless, the smaller diameter of the Nyquist semicircle for BNII indicates a lower corrosion resistance compared to CPII. This could be correlated with the more active surface presented by BNII as implied by the trend of OCP in Figure 1. The AFM morphological images of the corroded CPII and BNII specimens (Figure 4a and b, respectively) further illustrate the higher corrosion susceptibility of BNII, which manifests a much rougher surface in the test environment.

Polarization Measurements. Potentiodynamic polarization experiments were undertaken to distinguish the effect of nanocrystallization on the anodic and cathodic corrosion reactions in 0.1 M H₂SO₄. Typical potentiodynamic polarization curves of CPII and BNII illustrated in Figure 5 show that both specimens underwent active dissolution with no distinctive transition to passivation within the studied potential range. The value of the corrosion potential (E_{corr}) was also very slightly lowered from -506 mV for CPII to -511 mV in the case of BNII, and there was no marked variation in the polarization behavior of both specimens, especially in the vicinity of E_{corr}

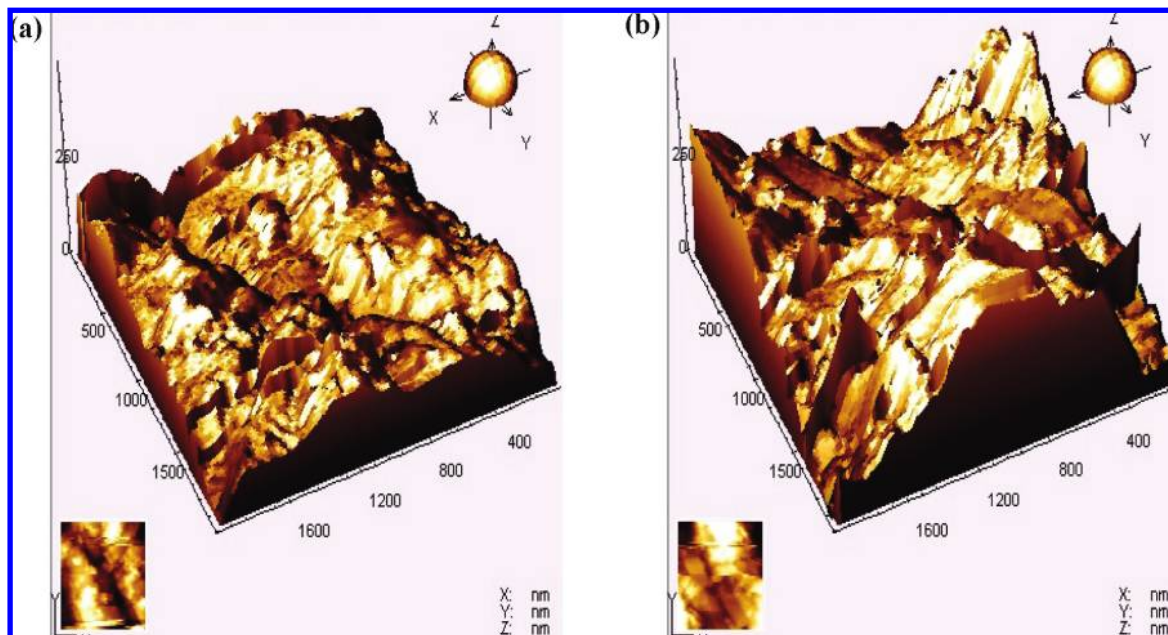


Figure 4. AFM images of the corroded (a) CPII and (b) BNII surfaces after 3 h immersion in uninhibited 0.1 M H_2SO_4 .

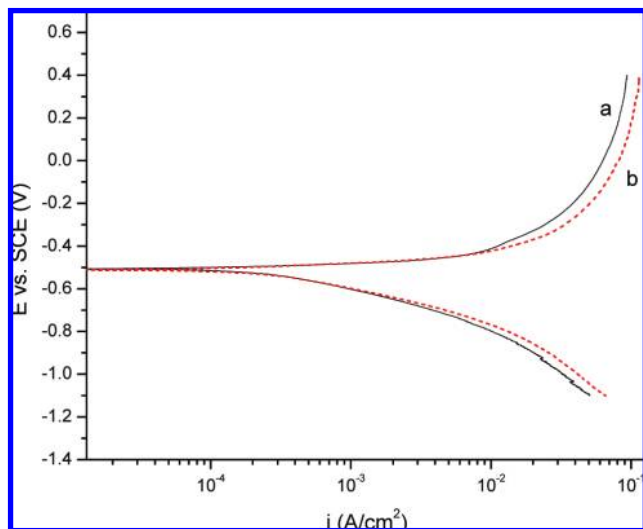


Figure 5. Polarization curves of CPII and BNII in 0.1 M H_2SO_4 without inhibitor. Measurements were carried out after 60 min of immersion.

(± 0.1 V). This could be related to the mean particle size of Fe atoms on the BNII (38.9 nm). Klabunde and Mulukutla²⁶ reported that for Fe metal nanoparticles, the ratio of surface to bulk (interior) atoms depends on the particle sizes, with 3 nm particles having about 50% of the atoms on the surface whereas 20 nm particles have about 10%. Nevertheless, nanocrystallization increased the kinetics of the anodic dissolution reaction at > -0.4 V (vs SCE) and that of the cathodic reaction at $E > -0.7$ V (vs SCE), thus increasing the corrosion current (i_{corr}) from 214 to 263 $\mu\text{A cm}^{-2}$. The enhancement in intrinsic chemical reactivity and hence corrosion rate can be explained vis-à-vis the differences in grain size and the subsequent structural modifications due to several factors including changes in crystal shape as well as distortions in the bonding patterns of the atoms.²⁶ It is worth mentioning that the large surface areas of nanostructured materials as well as the crystal shapes often present large concentrations of distinct defect sites including edges/corners and cavities, which provide active dissolution sites. In addition, the considerable volume of grain

boundaries, which for passive metals and alloys is often advantageous for outward diffusion of film forming elements, in the present case serves as fast diffusion conduits for the corrosive medium and hence promotes active dissolution of Fe. Rofagha et al.¹² also attributed the higher dissolution kinetics of nanocrystalline Ni–P compared to its polycrystalline counterpart in 0.1 M H_2SO_4 to the increased volume fraction of grain boundaries and defect sites. Other factors that could lead to corrosion acceleration include the presence of high stored energy and residual stress as well as extensive plastic deformation resulting from the severe rolling process.¹⁴

3.2. Electrochemical Corrosion Behavior of CPII and BNII in Inhibited Acid. Open-Circuit Potential Measurements.

From Figure 1 it is clear that introduction of TU into the acid solution led to a positive shift of OCP for both CPII and BNII, which corresponds to the formation of a protective layer of TU on both surfaces. It is interesting to note that the OCP gap between both specimens was maintained even in the presence of TU.

Impedance Measurements. Parts a and b of Figure 6 illustrate the effect of TU on the impedance response of CPII and exemplify respectively the Nyquist and Bode ($\log f$ vs phase angle) plots. Figure 7 gives similar plots for BNII. The Bode plots generally show single and narrow peaks, again indicating single time constants for the corrosion processes at the metal/solution interface in both the absence and presence of TU. However, for both CPII and BNII in inhibited solution, the Bode plots broaden at low frequencies and the peak heights increase significantly, indicating a more capacitive response of the interface due to the presence of TU. The Nyquist plots in the presence of TU again correspond to a single depressed semicircle, and as such the same equivalent circuit was used to fit the experimental data. The marked increase in the impedance parameters of both CPII and BNII in the presence of TU is associated with the corrosion inhibiting effect of the additive. R_{ct} values increased to 712.8 and 628.2 $\Omega\text{-cm}^2$ for CPII and BNII, respectively, while the corresponding values of the proportionality factor Q of CPE reduced to 4.46×10^{-5} and $3.61 \times 10^{-5} \mu\Omega^{-1} \text{s}^n \text{cm}^{-2}$. Such decrease in Q values normally results from a decrease in the dielectric constant and an increase

in the double layer thickness, which suggests that TU molecules are adsorbed on and modify the metal/electrolyte interface. This can be rationalized by considering the Helmholtz model

$$C_{dl} = \varepsilon \varepsilon_0 A / \delta \quad (3)$$

where ε is the dielectric constant of the medium, ε_0 the vacuum permittivity, A the electrode area, and δ the thickness of the protective layer. The smaller dielectric constant of the organic molecule compared to water as well as the increased the thickness of the double layer due to TU adsorption act to reduce the interfacial capacitance.

AFM images of the Fe surfaces corroded in the presence of TU are given in Figure 8 for CPII and BNII. We observe that both surfaces are smoother and significantly less corroded than the corresponding samples in uninhibited acid (Figure 4) due to the protective effect of adsorbed TU.

Polarization Measurements. Polarization experiments were also undertaken to gain some mechanistic insight on the effect of TU on the anodic and cathodic reactions of CPII and BNII. The resulting polarization curves are given in Figure 9. For both specimens, TU is seen to inhibit the anodic and cathodic reactions, reducing the corrosion current (i_{corr}) to 17.5 and 22.5 $\mu\text{A cm}^{-2}$ for CPII and BNII, respectively, while E_{corr} was not altered to any significant extent, which implies that the corrosion inhibition process is the same in both cases and is under mixed control.

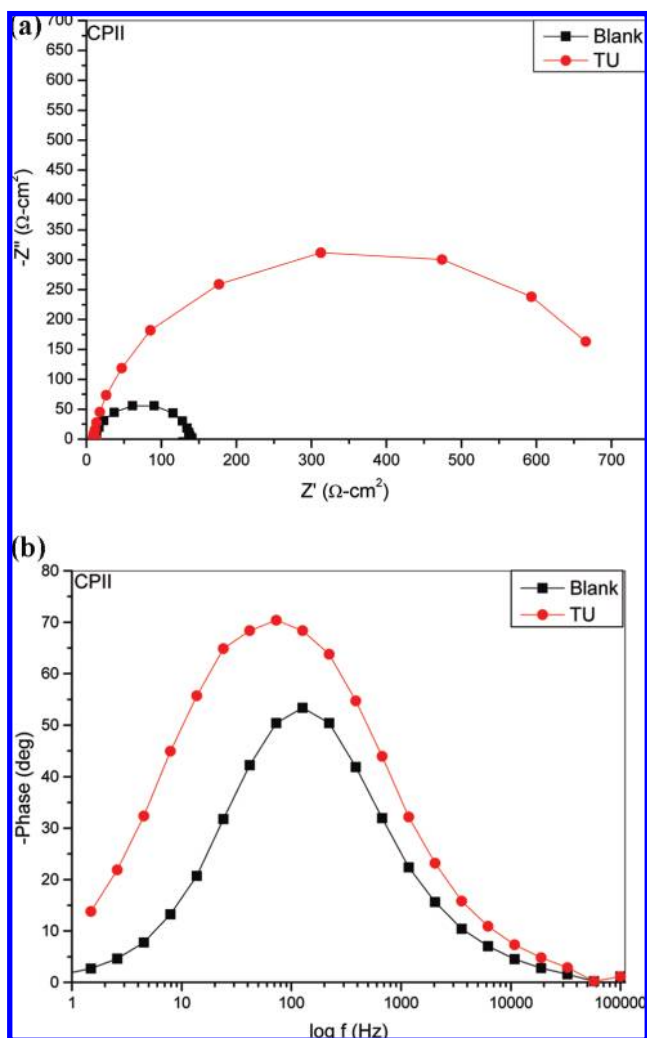


Figure 6. Electrochemical impedance plots of CPII in 0.1 M H_2SO_4 without and with 0.005 M TU: (a) Nyquist; (b) Bode phase angle plots.

Inhibition efficiency was calculated from the polarization data by

$$\eta_i\% = (1 - i'_{corr}/i_{corr}) \times 100 \quad (4)$$

where i'_{corr} and i_{corr} are the corrosion current densities in the presence and absence of TU. The calculated values show comparable inhibition efficiencies for TU on the corrosion of CPII ($\eta_i\% = 91.8\%$) and BNII ($\eta_i\% = 91.4\%$).

Again the net effects of TU on the corrosion process for both specimens seem somewhat similar, but a closer look reveals a striking discrepancy (which persisted in replicate runs of the experiments): For BNII, the anodic inhibiting effect of TU extends all through the studied potential range, unlike for CPII. This permits certain speculations regarding the effect of the nanocrystalline microstructure on inhibition mechanism.

First we consider the general inhibition mechanism of TU: Thiourea and its derivatives have been known for a long time to function as effective adsorption-type corrosion inhibitors for iron and steel in acidic media.^{20–22} The compound undergoes protonation with equilibrium constant (K_{eq}) 0.1:²²



$$K_{eq} = \frac{[\text{TUH}^+]}{[\text{TU}][\text{H}^+]} = 0.1 \quad (6)$$

TUH^+ and TU refer to the protonated and molecular species, respectively. For this study, $[\text{TUH}^+] \approx 0.05[\text{TU}]$, i.e., only about

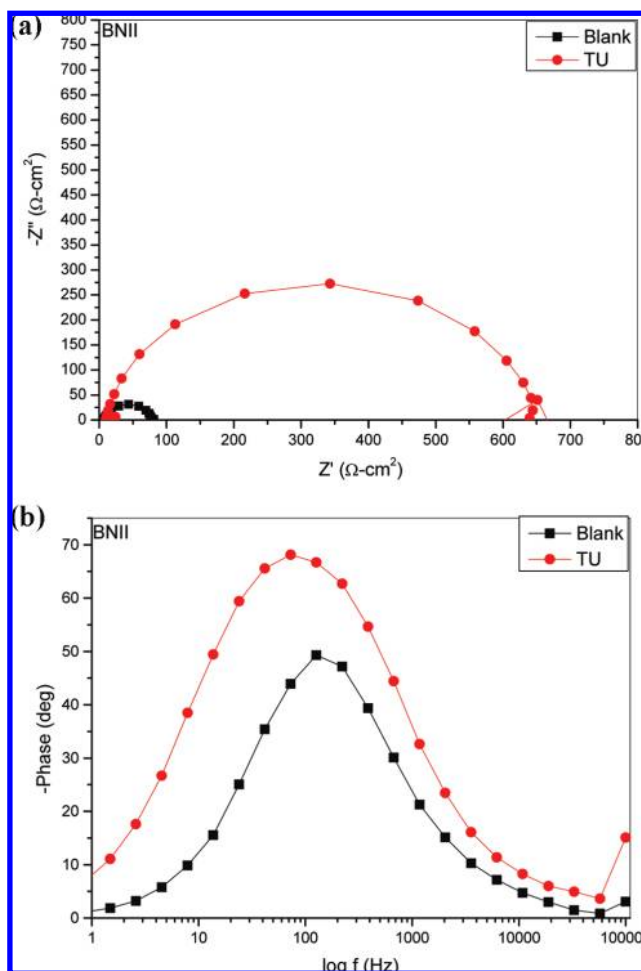


Figure 7. Electrochemical impedance plots of BNII in 0.1 M H_2SO_4 without and with 0.005 M TU: (a) Nyquist; (b) Bode phase angle plots.

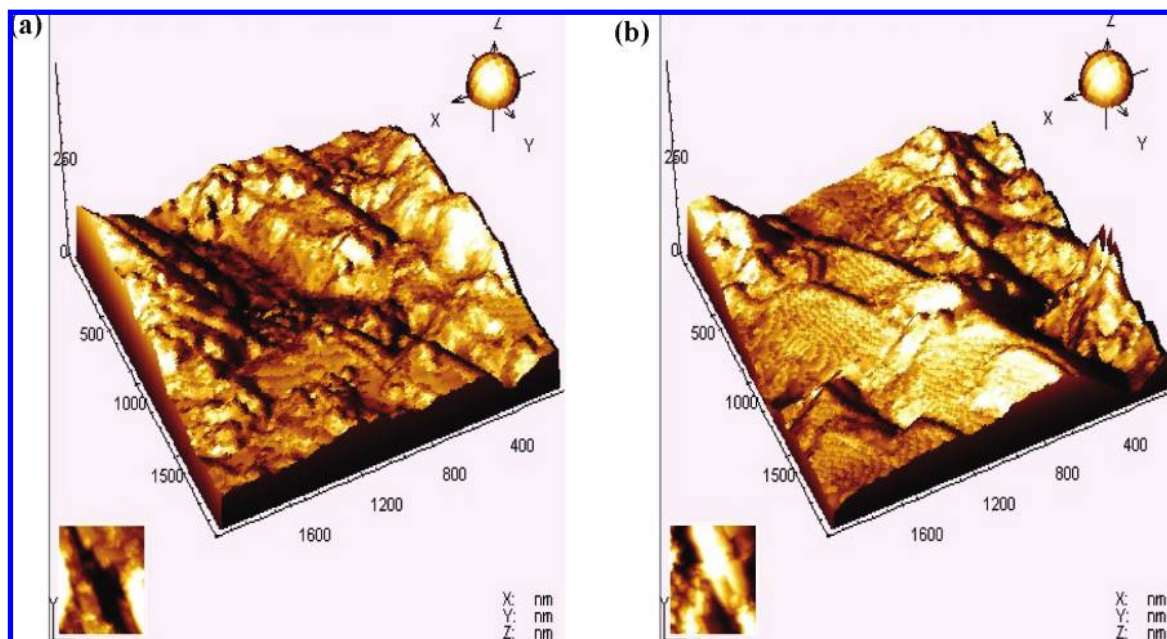


Figure 8. AFM images of the (a) CPII and (b) BNII surfaces after 3 h immersion in 0.1 M H_2SO_4 containing TU.

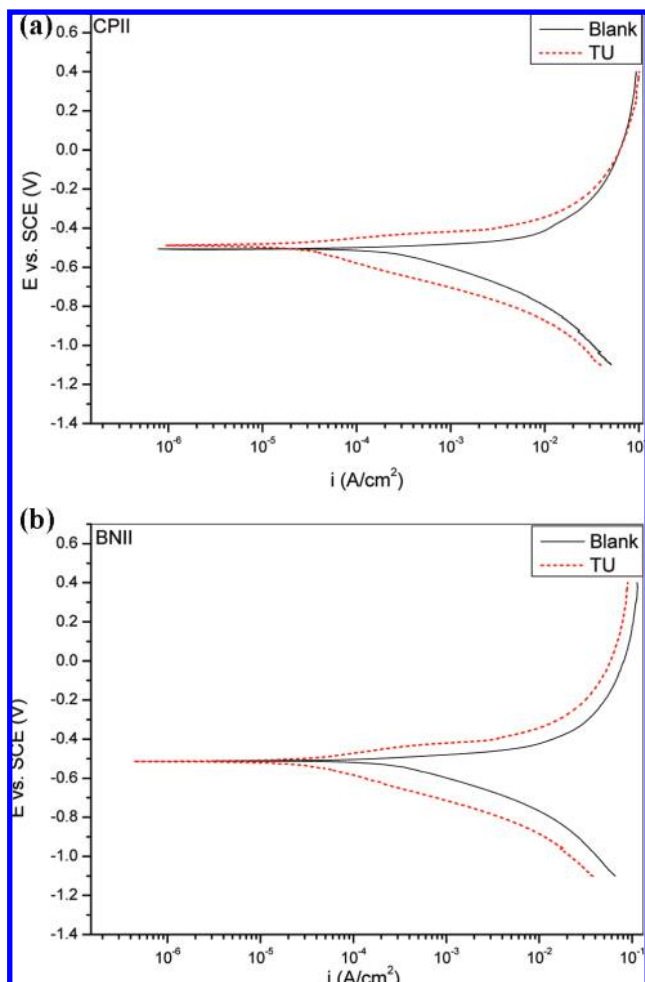


Figure 9. Polarization curves of (a) CPII and (b) BNII in 0.1 M H_2SO_4 without and with TU. Measurements were carried out after 60 min of immersion.

0.5% of the additive is protonated. Both protonated and molecular species could participate in the adsorption process, though to different extents depending on the prevailing experi-

mental conditions. According to the detailed mechanistic interpretation afforded by Ateya and co-workers,²² TU functions essentially by a geometric blocking effect in which the non-protonated species understandably exert a predominating influence, since their concentration is higher.

With respect to the influence of Fe microstructure, the present results as well as that of our earlier study using cysteine as an inhibitor¹⁷ point to the fact that the nanocrystalline surface favors inhibitor adsorption, particularly in the anodic domain. This could imply that the high defect population (grain boundaries, triple junctions, inclusions), which promote metal dissolution, also somehow provides an abundance of acceptor sites for the inhibitor. More specific experimental investigations are, however, necessary to ascertain whether preferential adsorption occurs at the grains, grain boundaries, or some other defect. All the same, it is noteworthy that preferential adsorption on edges, corners, and ridges has been reported for benzene on Cu (111) and dimethyl sulfoxide on Au (111).²⁶

A practical route to study the complex processes occurring between adsorbed inhibiting species and metal surfaces at the molecular level involves computer simulations of suitable models, and density functional theory (DFT) has been used widely in this regard.^{27–32} We have thus performed such calculations to model the adsorption structure of TU and hence provide some insight into the nature of TU interaction with the Fe surface. The TU structure was first subjected to Forcite geometry optimization using COMPASS force field and the Smart Minimize method by high convergence criteria.^{33,34} The optimized structure is given in Figure 10a, with total energy of -105.01 kcal/mol.

The electronic structure of TU, including the distribution of frontier molecular orbitals and Fukui indices, was assessed, with a view to establishing the active sites as well as local reactivity of the molecule. The simulations were performed by means of the DFT electronic structure program DMol³ using a Mulliken population analysis.^{35,36} Electronic parameters for the simulation include restricted spin polarization using the DND basis set and the Perdew–Wang (PW) local correlation density functional. The regions of highest electron density are often the sites at which electrophiles attack and represent the active centers, with

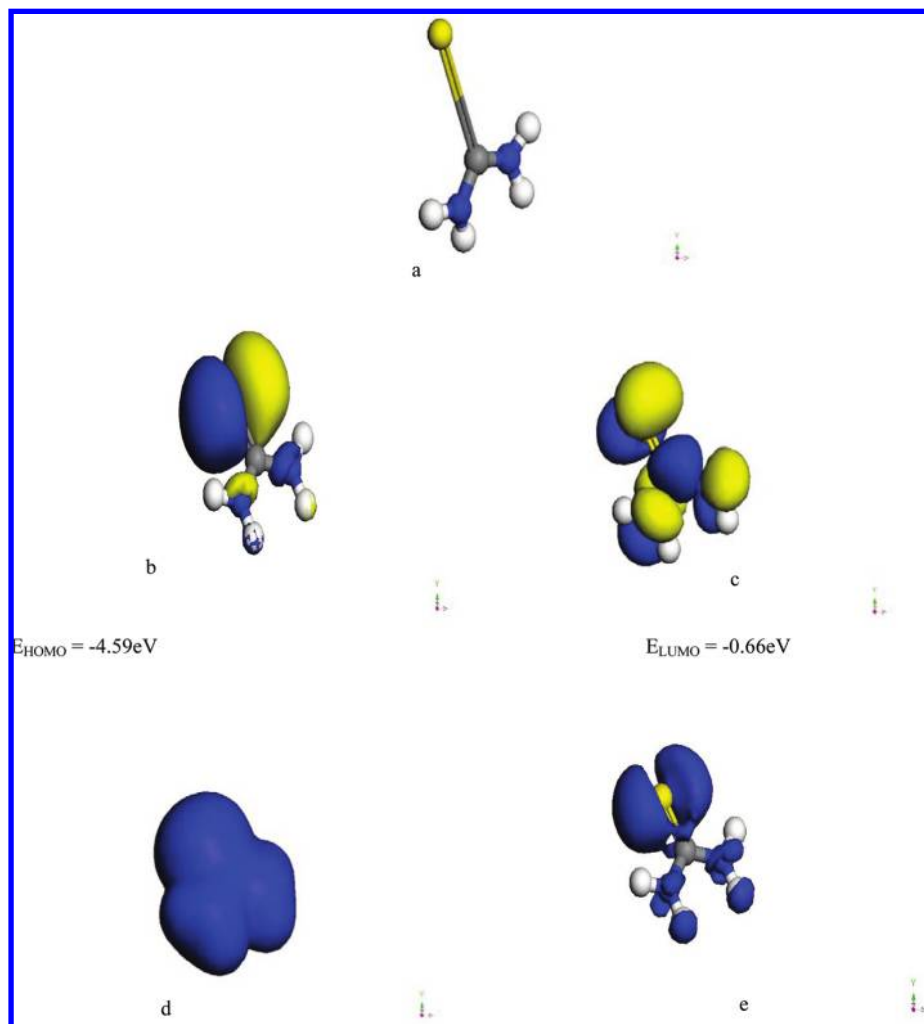


Figure 10. Electronic properties of TU: (a) optimized structure of TU, with total energy -105.01 kcal/mol ; (b) HOMO orbital; (c) LUMO orbital; (d) total electron density; (e) Fukui functions.

the utmost ability to bond to the metal surface. The highest occupied molecular orbital (HOMO) and lowest unoccupied molecular orbital (LUMO) of TU are presented in Figure 10b and c, respectively, with their corresponding energies. High values of E_{HOMO} can indicate the disposition of the molecule to donate electrons to an appropriate acceptor with vacant molecular orbitals.^{28–30} It is clear that the HOMO orbital of TU is made up predominantly of the S atom in the C=S group, with some contributions from the aminic nitrogens.

The total electron density (charge distribution) of the TU molecule (Figure 10d) shows three delocalization regions and corresponding charge densities (C=S $[-0.636]$; C–N; C–N $[-0.775]$), with the electron density saturated all around the molecule. Hence we should expect a flat-lying adsorption configuration, even though the HOMO orbital is saturated around the S atom.

The local reactivity of TU was analyzed by means of the Fukui indices (FI) to assess reactive regions in terms of nucleophilic and electrophilic behavior. The Fukui indices for electrophilic attack (f) were 0.632 and 0.020 for the S atom and the aminic nitrogens, respectively. Figure 10e shows that the Fukui functions of TU correspond with the HOMO locations, indicating the zones through which the molecule will be adsorbed on the Fe surface.

We have also undertaken molecular modeling of TU adsorption on the corroding metal surface to probe the

inhibition performance at the molecular level. Molecular dynamics (MD) simulation of the interaction between a single TU molecule and the Fe surface was performed using Forcite quench molecular dynamics in the MS Modeling 4.0 software to sample many different low energy configurations and identify the low energy minima. Calculations were carried out, using the COMPASS force field and the Smart algorithm, in a simulation box $17 \text{ \AA} \times 12 \text{ \AA} \times 28 \text{ \AA}$ with periodic boundary conditions to model a representative part of the interface, devoid of arbitrary boundary effects. The box was comprised of the Fe slab and a vacuum layer of 20 \AA height. The Fe crystal was cleaved along the (110) plane. Temperature was fixed at 350 K , with NVE (microcanonical) ensemble, with a time step of 1 fs and simulation time 5 ps . The system was quenched every 250 steps. Optimized structures of TU and the Fe surface were used for the simulation.

As earlier observed by Roque and co-workers³⁰ for Fe (100), we also found that the distribution of Fe atoms in the Fe (110) lattice also exhibits an electron deficiency in the corner Fe atoms and high electron density in the central atoms, which implies that the adsorption behavior of the corner atoms would be different from that of the central atoms, a phenomenon that could yield pronounced effects on the nanocrystalline microstructure.

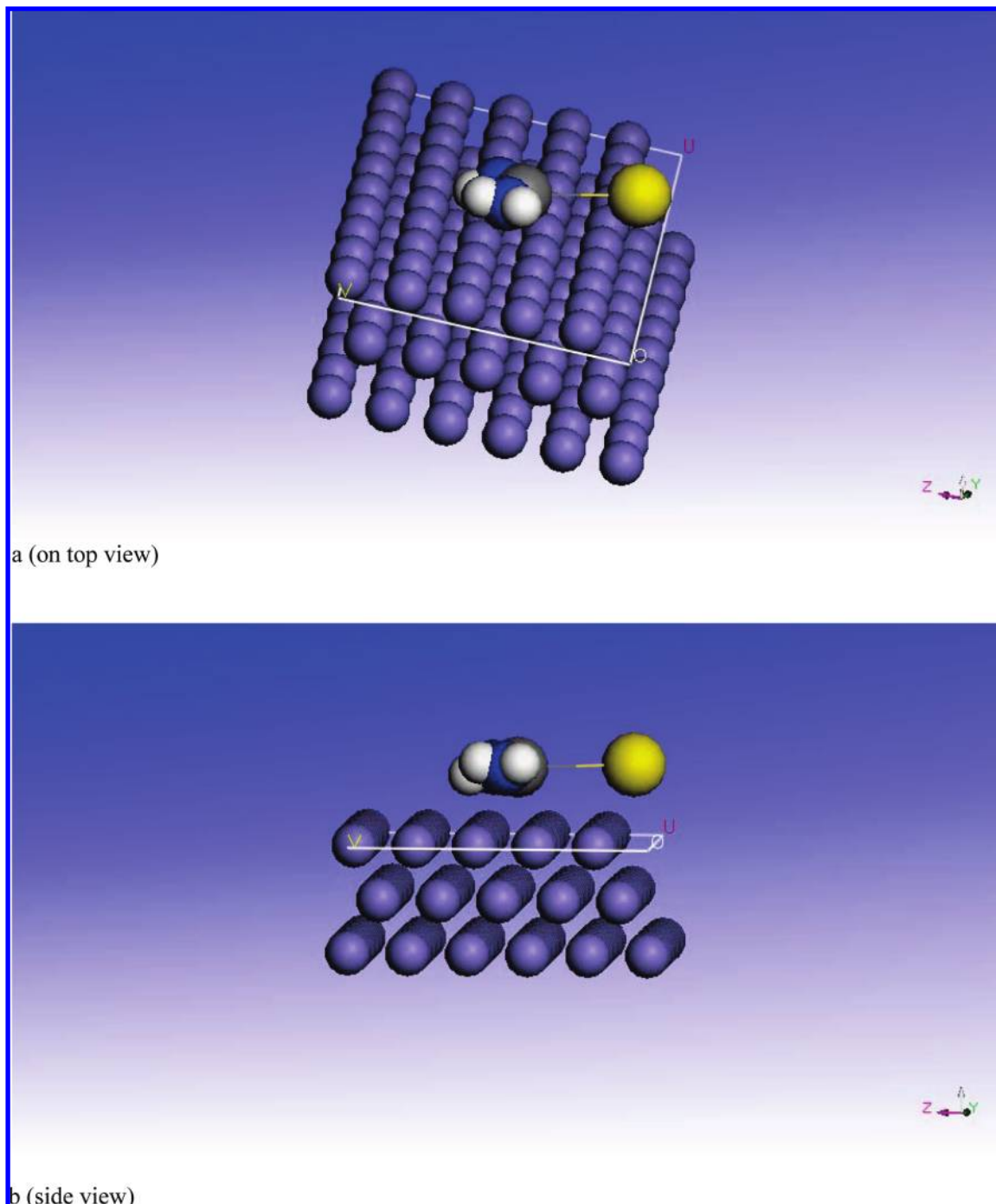


Figure 11. Molecular dynamics model of a single TU molecule adsorbed on Fe (110): (a) on-top view; (b) side view.

Figure 11 shows the optimized (lowest energy) adsorption model for a single TU molecule on the Fe (110) surface from our simulation. Solvent and charge effects have been neglected. TU is observed to maintain a flat-lying adsorption orientation on the Fe surface, in accord with the total electron distribution on the molecule (Figure 10d). Interestingly we also noticed that the TU molecule always assumed an orientation in which the S atom tends toward the edge Fe atoms rather than the bulk atoms (we observed this trend for different dimensions of the supercell). This behavior possibly implies that the electron-deficient corner Fe atoms exert greater affinity for and interact more strongly with the electron-rich S atom. This could account for the improved inhibiting effect of TU on BNII, with a higher population of edge and corner atoms.

3.3. Influence of KI on the Inhibiting Effect of TU. Figure 12 illustrates the impedance behavior of CPII (Figure 12a) and BNII (Figure 12b) in 0.1 M H_2SO_4 containing KI, TU + KI, and TU (for comparison). KI added to 0.1 M H_2SO_4 with no added TU increases R_{ct} compared to the blank, which corresponds to an inhibiting effect. We, however, observe that R_{ct} for the different systems increased in the order $\text{KI} < \text{TU} + \text{KI} < \text{TU}$. In other words, corrosion rates of both CPII and BNII were lowest in the solutions containing only TU. This indicates that KI diminished rather than enhanced the inhibition efficiency of TU. Similar conclusions were also drawn from the polarization curves (not shown).

The above observations suggest possible modifications in the chemical nature of inhibitor species adsorbed on the Fe/

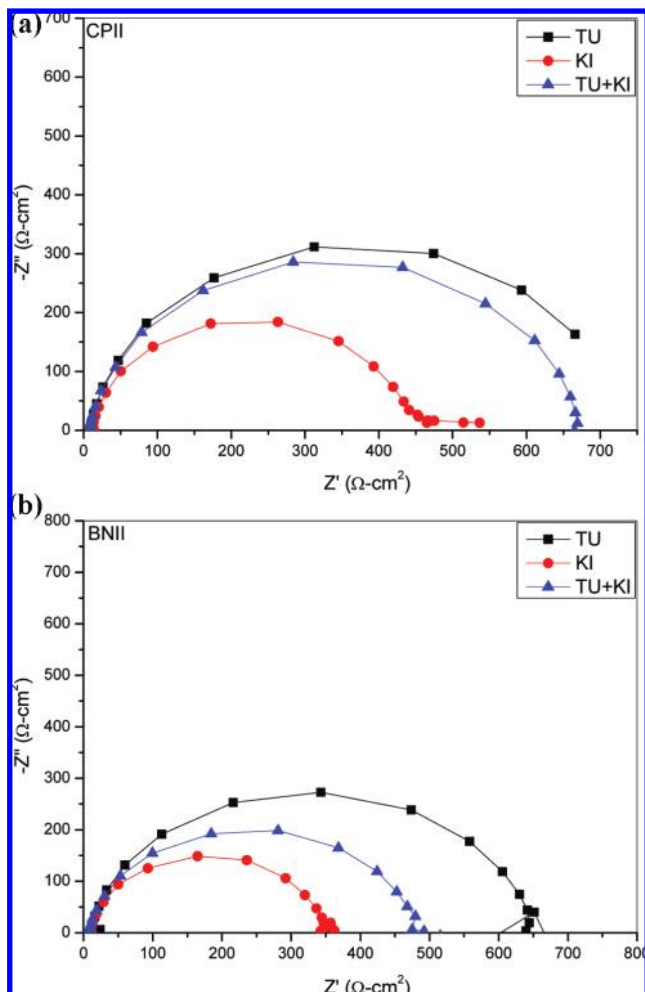


Figure 12. EIS Nyquist plots of (a) CPII and (b) BNII in 0.1 M H₂SO₄ containing TU, KI, and TU + KI.

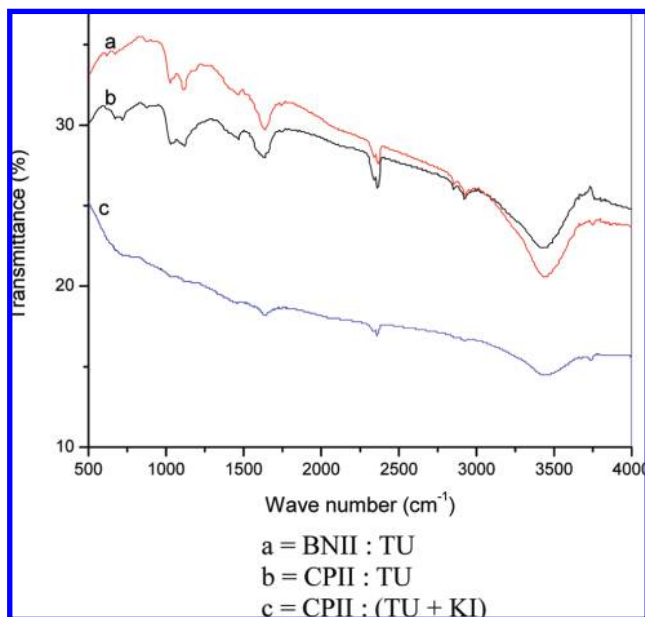
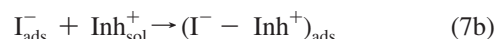


Figure 13. FTIR spectra of TU on CPII (a) and BNII (b) as well as of TU + KI on CPII (c).

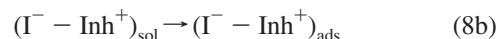
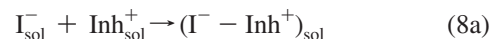
acid interface in the presence of KI, which was subsequently analyzed using infrared spectroscopy. Figure 13 shows that the FTIR spectra of the interfacial species formed on CPII (a) and BNII (b) immersed in TU are quite identical, indi-

cating that the same species were present on the surfaces of both specimens (TU_{ads}). The FTIR spectra obtained in TU + KI (c) were, however, very different from that in TU. This signifies that the interfacial species become chemically altered in the presence of KI.

Two mechanisms could account for this transformation of TU_{ads}: TU is either quickly chemically transformed on the Fe surface or in solution in the TU + KI medium. Relating these to the ion-pair interactions leading up to inhibitor–halide synergism, the former case somewhat resembles the more widely acceptable situation in which ion-pair formation occurs directly on the metal surface:^{4,5}



This, however, should not lead to pronounced chemical changes to TU as revealed in Figure 13 since the interactions are purely electrostatic. The latter circumstance in which chemical transformation of TU takes place in solution resembles ion-pair formation in solution and represents the actual situation in this study, though the observed chemical transformation of TU again precludes actual formation of ion-pairs:



I_{sol}^- , $\text{Inh}_{\text{sol}}^+$, and $(\text{I}^- - \text{Inh}^+)_{\text{sol}}$ represent the inhibitor, halide ion, and ion-pair, respectively, in the bulk of the solution, while I_{ads}^- , $\text{Inh}_{\text{ads}}^+$, and $(\text{I}^- - \text{Inh}^+)_{\text{ads}}$ refer to the same species in the adsorbed state. It seems that KI reacts more readily with TU rather than getting adsorbed on the Fe surface, for which we had visual evidence via the immediate decoloration of the yellow KI solution (due to oxidation of I^{2-} to I_2) on addition of TU. This results in the formation of new reaction products that get adsorbed on the Fe surface and accounts for the modification of the infrared spectra in TU + KI media, including the observed lower inhibition efficiency compared to TU alone.

Interestingly, a survey of the literature reveals a number of reports on the reactions of TU with KI. Rabai and Beck³⁷ reported that I_2 oxidizes TU in several steps, the end products being SO_4^{2-} , NH_4^+ , and CO_2 . Prakash et al.³⁸ reported the formation of a thiourea complex of tetrakis thiourea potassium iodide by the reaction between TU and KI. Though we did not attempt exact characterization of the KI + TU reaction products in this study, it is reasonable to suggest that this reaction interferes with the inhibiting effect of TU. Hence in investigating halide–inhibitor synergism, due consideration should be given to their possible chemical reaction in solution, which could manifest as either a minor side reaction (which may not be immediately obvious) or the major reaction as observed in this study. Consequently, manifestations of antagonistic effects may not necessarily be due to competitive adsorption as often inferred, but could rather be due to chemical reactions between the additives as shown in the present study, or even withdrawal of adsorbed halide ions from the metal surface into the solution due to strong interaction with the organic cation as reported earlier by Murakawa and co-workers.¹

4. Conclusions

Bulk nanocrystallization effected by the severe rolling technique diminished the corrosion resistance of ingot iron in 0.1 M H₂SO₄ solution by accelerating the kinetics of the anodic metal dissolution process. Thiourea (TU) exerted comparable

corrosion inhibiting effects for both the polycrystalline (CPII) and the nanocrystalline (BNII) iron samples, despite the higher corrosion susceptibility of the latter. Thus both corrosion and corrosion inhibition mechanisms were affected by the microstructure of the sample. Potassium iodide diminished the inhibition performance of TU by chemically modifying the nature of the interfacial species responsible for the inhibiting effect. Molecular dynamics simulation was used to model the adsorption of a single TU molecule on the surface of iron.

Acknowledgment. E.E.O. is on a TWAS-UNESCO Associateship appointment. Financial support from the National Natural Science Foundation of China under contract nos. 50501023 and 50771098 is gratefully acknowledged. J.B.L. is acknowledged for useful discussion.

References and Notes

- (1) Murakawa, T.; Kato, T.; Nagaura, S.; Hackerman, N. *Corros. Sci.* **1968**, *8*, 483.
- (2) Wu, Y. C.; Zhang, P.; Pickering, H. W.; Allara, D. L. *J. Electrochem. Soc.* **1993**, *140*, 2791.
- (3) Oguzie, E. E. *Mater. Chem. Phys.* **2004**, *87*, 214.
- (4) Oguzie, E. E.; Li, Y.; Wang, F. H. *J. Colloid Interface Sci.* **2007**, *310*, 90.
- (5) Shibli, S. M. A.; Saji, V. S. *Corros. Sci.* **2005**, *47*, 2213.
- (6) Popova, A.; Sokolova, E.; Raicheva, S.; Christov, M. *Corros. Sci.* **2003**, *45*, 33.
- (7) Mu, G. N.; Li, X.; Li, F. *Mater. Chem. Phys.* **2004**, *86*, 59.
- (8) Bouklah, N.; Hammouti, B.; Aouniti, A.; Benkaddour, M.; Bouyanzer, A. *Appl. Surf. Sci.* **2006**, *252*, 6236.
- (9) Wang, X. Y.; Li, D. Y. *Electrochim. Acta* **2002**, *47*, 3939.
- (10) Kwok, C. T.; Cheng, F. T.; Man, H. C.; Ding, W. H. *Mater. Lett.* **2006**, *60*, 2419.
- (11) Youssef, Kh. M. S.; Koch, C. C.; Fedkiw, P. S. *Corros. Sci.* **2004**, *46*, 51.
- (12) Rofagha, R.; Langer, R.; El-Sherik, A. M.; Erb, U.; Palumbo, G.; Aust, K. T. *Scr. Metall. Mater.* **1991**, *25*, 2867.
- (13) Mishra, R.; Balasubramaniam, R. *Corros. Sci.* **2004**, *46*, 3019.
- (14) Wang, S. G.; Shen, C. B.; Long, K.; Yang, H. Y.; Wang, F. H.; Zhang, Z. D. *J. Phys. Chem. B* **2005**, *109*, 2499.
- (15) Wang, S. G.; Shen, C. B.; Long, K.; Zhang, T.; Wang, F. H.; Zhang, Z. D. *J. Phys. Chem. B* **2006**, *110*, 377.
- (16) Shen, C. B.; Wang, S. G.; Yang, H. Y.; Long, K.; Wang, F. H. *Electrochim. Acta* **2006**, *52*, 3950.
- (17) Oguzie, E. E.; Wang, S. G.; Li, Y.; Wang, F. H. *J. Solid State Electrochem.* **2008**, *12*, 721.
- (18) Shetty, S. D.; Shetty, P.; Nayak, H. V. S. *Mater. Lett.* **2007**, *61*, 2347.
- (19) Shen, C. B.; Han, D. Y.; Ding, Z. M. *Mater. Chem. Phys.* **2008**, *109*, 417.
- (20) El-Egamy, S. S. *Corros. Sci.* **2008**, *50*, 928.
- (21) Tang, L. N.; Wang, F. P. *Corros. Sci.* **2008**, *50*, 1156.
- (22) Ateya, B. G.; El-Anadoul, B. E.; El-Mizamy, F. M. *Corros. Sci.* **1984**, *24*, 497.
- (23) Grips, V. K. W.; Selvi, V. E.; Barshilia, H. C.; Rajan, K. S. *Electrochim. Acta* **2006**, *51*, 3461.
- (24) Moretti, G.; Guidi, F.; Grion, G. *Corros. Sci.* **2004**, *46*, 387.
- (25) Lopez, D. A.; Simison, S. N.; de Sanchez, S. R. *Electrochim. Acta* **2003**, *48*, 845.
- (26) Klabunde, K. J.; Mulukutla, R. S. *Nanoscale Materials in Chemistry*; John Wiley and Sons Inc.: New York, 2001; p 223.
- (27) Khaled, K. F. *Electrochim. Acta* **2008**, *53*, 3484.
- (28) Guo, W.; Chen, S.; Feng, Y.; Yang, C. *J. Phys. Chem. C* **2007**, *117*, 3109.
- (29) Turcio-Ortega, D.; Pandiyan, T.; Cruz, J.; Garcia-Ochoa, E. *J. Phys. Chem. C* **2007**, *111*, 9853.
- (30) Roque, J. M.; Pandiyan, T.; Cruz, J.; Garcia-Ochoa, E. *Corros. Sci.* **2008**, *50*, 614.
- (31) Cui, G.; Ke, X.; Liu, H.; Zhao, J.; Song, S.; Shen, P. K. *J. Phys. Chem. C* **2008**, *112*, 13546.
- (32) Xia, S.; Qui, M.; Yu, L.; Liu, F.; Zhao, H. *Corros. Sci.* **2008**, *50*, 2021.
- (33) Casewit, C. J.; Colwell, K. S.; Rappé, A. K. *J. Am. Chem. Soc.* **1992**, *114*, 10035.
- (34) Casewit, C. J.; Colwell, K. S.; Rappé, A. K. *J. Am. Chem. Soc.* **1992**, *114*, 10046.
- (35) Delley, B. *J. Chem. Phys.* **1990**, *92*, 508.
- (36) Delley, B. *J. Chem. Phys.* **2000**, *113*, 7756.
- (37) Rabai, G.; Beck, M. T. *J. Chem. Soc., Dalton Trans.* **1985**, 1669.
- (38) Prakash, J. T. J.; Vijayan, N.; Kumararaman, S. *Cryst. Res. Technol.* **2008**, *43*, 423.